GEOPHYSICS, VOL. 71, NO. 4 (JULY-AUGUST 2006); P. SI95–SI102, 8 FIGS.
10.1190/1.2213951



# Improved Green's functions for passive-source structural studies

Jean-Philippe Mercier[1], Michael G. Bostock[1], and Adam M. Baig[1]

## ABSTRACT

Over the past two decades, teleseismic receiver functions have proved to be a useful tool to investigate crustal structure. Because they represent a first-order approximation to the *S*-wave component of the teleseismic-*P* Green's function, receiver functions provide valuable information on physical properties related to shear modulus. However, the implicit use of the *P*-component seismogram as a proxy for the source precludes the recovery of information on discontinuous structure involving contrasts in compressional modulus. By deconvolving improved estimates of complex source time functions generated by earthquakes, one may move beyond the conventional receiver function paradigm to a more accurate approximation of the earth's Green's function. Using a new deconvolution method, we present estimates of the *P*-component of the teleseismic-*P* Green's functions at several stations of the Canadian National Seismic Network (CNSN) that clearly show the receiver-side pure *P*-wave crustal multiple. The identification and characterization of these signals in studies of the lithosphere will afford better constraints on subsurface lithology and represent a narrowing of the gap between active- and passive-source seismic imaging.

## INTRODUCTION

For the past few decades, teleseismic receiver functions have provided valuable information on crust and lithospheric structure. In the mid-1960s, Phinney (1964) proposed that the spectral ratio of horizontal/vertical component seismograms (that is, the frequency domain receiver function) could be used to gauge the effect of crustal layering on frequency-dependent polarization. More than a decade later, Burdick and Langston (1977) investigated the time-domain response of impulsive, plane-wave sources at near-vertical incidence and demonstrated that a full suite of forward- and back-scattered phases could be exploited to better constrain crustal structure. Shortly after, Langston (1979) introduced the time-domain receiver function as a means of recovering first-order, *P*-to-*S* scattering (note also parallel work by Vinnik (1977) on transition zone discontinuities) and thereby generalized earlier work to complex source-time functions. Inspired by this work, Owens and Zandt (1985) and countless others subsequently exploited the receiver function methodology to examine the continental crust-mantle boundary by coupling receiver-function observations with forward-modeled synthetic seismograms for geologically realistic models. They demonstrated that receiver functions could supply information complementary to that produced using active-source seismic methods.

Most early teleseismic crustal studies employing receiver functions focused on characterizing the forward-scattered converted $P_Ds$ phase (where a given discontinuity is designated by *D*) and considered free-surface reflected multiples (or back scattering) as a source of noise (see Figure 1 for details). The study of the isolated $P_Ds$ phase suffers from at least two important limitations. First, there is a significant trade-off between depth to a subsurface discontinuity and the overlying velocity profile. Second, the use of this single phase with a narrow, near-vertical sampling in incidence angle provides information only on the relative *S*-velocity contrast across an interface, with no constraint placed on either compressional modulus or density. The timing of free-surface multiples can be used to address the first limitation to a certain degree. For example, Zandt and Ammon (1995) investigated bulk crustal composition using estimates of average Poisson's ratio and crustal thickness. These quantities were derived using measured times of both forward- and free-surface-reflected, back-scattered waves (that is, $Pp_Ds$ and $Ps_Ds$). This approach has been subsequently generalized and rendered more robust through waveform stacking by Zhu and Kanamori (2000). The amplitudes of the multiples $Pp_Ds$ and $Ps_Ds$ also afford some sensitivity to density contrast but remain insensitive to compressional modulus.

Most recently, efforts have been directed toward exploiting receiver functions in the delineation of 2D and 3D earth structure using migration/inversion methods such as those routinely employed in hydrocarbon exploration (Revenaugh, 1995; Dueker and Sheehan, 1997; Bostock et al., 2001; Poppeliers and Pavlis, 2003). The tele-

Manuscript received by the Editor March 31, 2005; revised manuscript received July 21, 2005; published online August 17, 2006.
[1]Department of Earth and Ocean Sciences, University of British Columbia, 6339 Steres Road, Vancouver, British Columbia, Canada V6T 1Z4. E-mail: jmercier@eos.ubc.ca; bostock@eos.ubc.ca; abaig@eos.ubc.ca.

seismic application holds the advantage that the full vector wavefield generally is recorded, thereby allowing, at least in principle, recovery of a spatially varying suite of elastic parameters. Incorporation of both forward- and back-scattered energy from classic receiver functions within an imaging/inversion formulation permits the estimation of two isotropic elastic parameters, namely, *S*-velocity and density, or combinations thereof. Information on subsurface *P*-impedance structure is present also within the recorded wavefield, but its extraction therefrom will demand that we move beyond the classic receiver function to a more fundamental quantity, that is, the earth's Green's function. This task, in turn, requires that we are better able to remove the effect of the earthquake source-time function.

In this paper, we demonstrate application of a method described by Baig et al. (2005) that relies on certain spectral properties of the teleseismic wavefield to recover the *P*-component of the Green's function. First we provide a motivation and brief explanation of the method, including its multichannel implementation. Then we present simple numerical simulations of Green's functions that identify the key elements of teleseismic scattering from lithospheric discontinuities. We use these simulations to help interpret deconvolved data that clearly demonstrate the retrieval of improved Green's function estimates, computed for three stations of the CNSN.

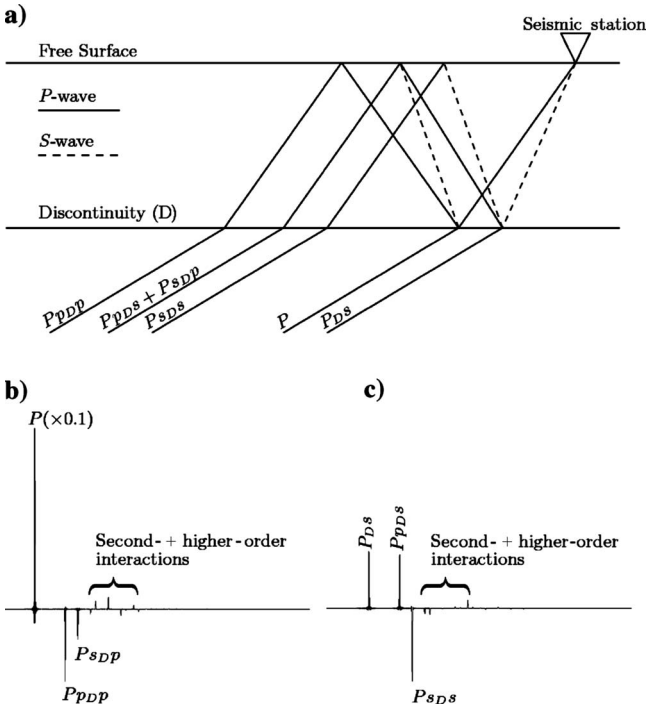


Figure 1. (a) Raypaths for first-order scattered phases in a layer over half-space model; (b) and (c) show synthetic *P*- and *SV*-components for incident impulsive *P*-wave generated for a model that is a Poisson's solid featuring a 36-km thick crust with *P*-velocity $\alpha_c = 6.5$ km s$^{-1}$ and density $\rho_c = 2.7$ g cm$^{-3}$ overlying a mantle half-space with *P*-velocity $\alpha_m = 8.1$ km s$^{-1}$ and density $\rho_m = 3.3$ g cm$^{-3}$. The wavefield is characterized by a constant horizontal slowness of 0.06 s km$^{-1}$.

## METHODOLOGY

This section outlines a new deconvolution technique (Baig et al., 2005) that allows recovery of the teleseismic-*P* Green's function and, in particular, its *P*-component. The method is based on recognizing that the latter quantity is minimum-phase (Sherwood and Trorey, 1965; Bostock, 2004) and, consequently, that it can be reconstructed uniquely and completely from its amplitude spectrum alone (note here that no assumptions are made concerning the nature of the source spectrum, only that of the Green's function). Physically, the minimum-phase property stems from the fact that the incident or ballistic contribution to the teleseismic-*P* Green's function can be characterized by a single, quasi-planar wavefront that contains more energy at all frequencies than the scattered waves that follow in its wake. The validity of this assumption is reaffirmed by the success of receiver function analysis, which implicitly relies on the minimum-phase property. Because the phase spectrum of a minimum-phase time series is uniquely prescribed by its amplitude spectrum, the source/Green's function deconvolution problem can be simplified to the isolation of the respective amplitude spectra.

Our initial approach for this problem relied on the use of the cross spectrum of two seismograms sharing a common component, e.g., two components of the same three-component seismogram. This approach was motivated by recognizing that the source, which represents that convolutional element common to both seismograms, is represented within the zero-phase component of the cross spectrum. Consequently, if we were able to extract the zero-phase component of the cross spectrum, we would have an estimate of the source spectrum that is accurate to the extent that no common (i.e., zero-phase) signal exists in the underlying Green's function correlogram. In theory, as explained by Baig et al. (2005), there are methods for achieving this zero-phase/non-zero-phase component separation. In practice, we found that noise, coupled with uncertainties in the length of effective support interval occupied by the Green's function crosscorrelogram, render those approaches less effective than the alternative blind deconvolution method that we describe below.

### Source estimation

In the approach adopted here, we consider a three-component teleseismic-*P* recording as resulting from the convolution of a band-limited source with respective components of a Green's function that possess statistically white amplitude spectra. The motivation for this breakdown stems from the absorptive properties of the mantle, which tend to attenuate higher frequencies of the teleseismic wavefield, and from our expectation that the receiver-side impulse response of the crust and lithospheric mantle is full band. Consider, for example, the cross spectrum of two components of a single three-component seismogram,

$$P(\omega)V^*(\omega) = |S(\omega)|^2 G^P(\omega)G^{V*}(\omega), \qquad (1)$$

where $P(\omega)$ and $V(\omega)$ are the *P*- and *SV*-components of the seismogram in the frequency domain, $G^P(\omega)$ and $G^V(\omega)$ are the corresponding components of the Green's function, $|S(\omega)|^2$ is the power spectrum of the source, and * denotes complex conjugation. The transformation from particle displacement into estimates of the up-going *P*-, *SV*-, and *SH*-components of motion can be accomplished by coordinate rotation (Vinnik, 1977) or by assuming propagation through a laterally homogeneous earth model (Kennett, 1991). The accuracy of this transformation is not important except insofar as energy in the incident *P*-wave is effectively isolated to the

*P*-component. This isolation improves the likelihood that the minimum-phase assumption will be honored for this component. We may restore the recovered Green's function to standard Cartesian displacement through the corresponding inverse transformation after completing deconvolution.

The simplest means of estimating the source spectrum might be to assume that the amplitude spectrum of the individual Green's function components is constant in frequency and, thus, that the source power spectrum $|S(\omega)|^2$ is equivalent to the amplitude spectrum of the seismogram cross-correlogram $|P(\omega)V^*(\omega)|$. In synthetic tests comprising simple, horizontally layered models (Baig et al., 2005), we gauged the accuracy of this approach by examining the quality of reproduction of the recovered Green's function crosscorrelogram [i.e., the inverse Fourier transform of $G^P(\omega)G^{V*}(\omega)$]. This estimate generally possesses many of the features of the true crosscorrelogram, especially at negative lags, which are dominated by interaction of the incident *P*-pulse with the first-order *P*-to-*S*-conversions. This observation is perhaps not surprising, given that it is the quantity $P^*(\omega)V(\omega)$ that appears in the numerator of a standard, least-squares, frequency-domain, receiver-function deconvolution. The reproduction at positive lags is poorer as the signal levels are lower because the dominant, incident-*P* arrival does not contribute to this portion of the crosscorrelogram. Lowest-order scattering interactions are identifiable, but so are a small number of spurious artificial arrivals (see Figure 2) that could undermine confidence in geologic interpretations.

A less extreme approach is to assume that the Green's function components possess spectra that are statistically white (as opposed to strictly constant), whereas the source power spectrum is band-limited, and then to estimate the latter quantity by spectral smoothing (Claerbout, 1992). In our experiments, we found that a simple, time-domain, low-pass Gaussian filter ($e^{(t^2/t_c^2)}$, where $t_c$ is the cutoff time) applied to the amplitude spectrum of the crosscorrelogram, works as well as any other for smoothing purposes. The choice of the cutoff time $t_c$ influences the quality of the deconvolution. In the limit that $t_c$ extends to the full length of the signal, the Green's function spectrum becomes constant. Then, the recovered Green's function crosscorrelogram ($\mathcal{F}^{-1}\{|G^P(\omega)G^{V*}(\omega)|e^{\phi(P(\omega)V^*(\omega))}\}$, where $\mathcal{F}^{-1}$ denotes inverse Fourier transformation and $\phi(P(\omega)V^*(\omega))$ is the phase of the original crosscorrelogram) approaches that of a constant amplitude spectrum, replete with spurious arrivals as discussed above. As $t_c$ decreases, the amount of smoothing increases, and the spurious arrivals diminish in size, leaving the lowest-order scattering interactions more clearly identifiable above ambient noise levels. At very short $t_c$, the source spectrum whitens, and the recovered Green's function correlogram approaches that of the raw seismograms. From experiment, we found that the choice of optimal $t_c$ corresponds to inclusion of the main lobe of the zero-phase quantity $\mathcal{F}^{-1}\{|G^P(\omega)G^{V*}(\omega)|\}$ with secondary lobes strongly attenuated. The effect of the length of $t_c$ is shown in Figure 3.

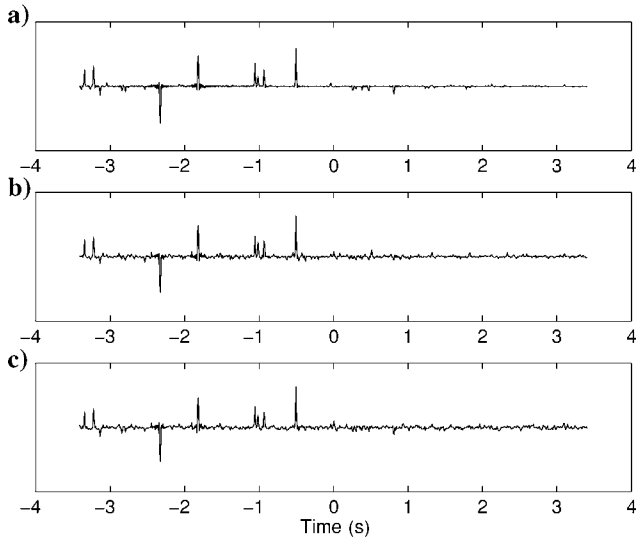


Figure 2. Comparison of original crosscorrelograms: (a) true $\mathcal{F}^{-1}\{G^P(\omega)G^{V*}(\omega)\}$ crosscorrelogram; (b) and (c) estimated $\mathcal{F}^{-1}\{G^P(\omega)\times G^{V*}(\omega)\}$ crosscorrelograms using flat spectrum and spectral smoothing, respectively. Note the good correspondence at negative lags for both estimates and a better correspondence for spectral smoothing at positive lags.

## Deconvolution

To improve our estimates of the source and teleseismic Green's function spectra, we exploit the availability of multiple recordings and employ the multichannel spectral deconvolution approach originally presented by Andrews (1986). We consider a collection of three-component seismograms sharing the same impulse responses (that is, the same source-receiver geometry) but characterized by different source-time functions. This approach contributes to increased redundancy and improved quality of the Green's function spectral reconstruction.

For a single station and a set of $M$ independent sources, we have $3 \times M$ convolution equations which can be written for amplitude spectra in the frequency domain as

$$\mathbf{P}_m(\omega) = |S_m(\omega)|\mathbf{G}(\omega), \tag{2}$$

where $\mathbf{P}_m(\omega) = [|P_m(\omega)|, |V_m(\omega)|, |H_m(\omega)|]^T$ is the $m$th three-component seismogram, $\mathbf{G}(\omega) = [|G^P(\omega)|, |G^V(\omega)|, |G^H(\omega)|]^T$ is the three-component Green's function, and $S_m(\omega)$ is the $m$th source.

Transformation of the system in equation 2 into the log-spectral domain allows us to linearize it as

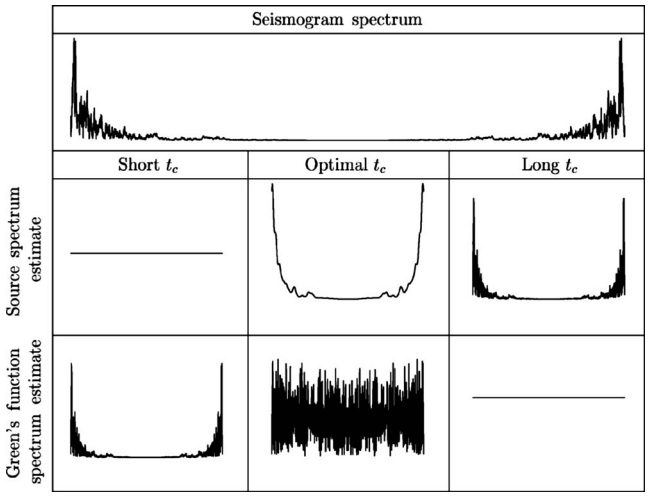


Figure 3. Effect of the cutoff time, or spectral smoothing parameter, on the source and Green's function amplitude spectrum estimate.

$$\log\{\mathbf{P}_m(\omega)\} = \log\{|S_m(\omega)|\}\mathbf{1} + \log\{\mathbf{G}(\omega)\}, \tag{3}$$

where $\mathbf{1} = [1,1,1]^T$. These equations are then augmented with source estimates $\widetilde{S}_m$, obtained by the approach of the previous section to yield a highly overdetermined system:

$$\begin{bmatrix} \mathbf{I}_3 & \mathbf{1} & \cdots & 0 \\ 0 & \mathbf{1} & \cdots & 0 \\ \vdots & \vdots & \ddots & \vdots \\ \mathbf{I}_3 & 0 & \cdots & \mathbf{1} \\ 0 & 0 & \cdots & \mathbf{1} \end{bmatrix} \begin{bmatrix} \log\{\mathbf{G}(\omega)\} \\ \log\{|S_1(\omega)|\} \\ \vdots \\ \log\{|S_M(\omega)|\} \end{bmatrix} = \begin{bmatrix} \log\{\mathbf{P}_1(\omega)\} \\ \log\{|\widetilde{S}_1(\omega)|\} \\ \vdots \\ \log\{\mathbf{P}_M(\omega)\} \\ \log\{|\widetilde{S}_M(\omega)|\} \end{bmatrix}, \tag{4}$$

where $\mathbf{I}_3$ is the $3 \times 3$ identity matrix.

The solution of equation 4 recovers an improved estimate of the three-component teleseismic Green's functions spectrum (see Baig et al., 2005). By invoking the minimum-phase property of the *P* impulse response, we can reconstruct the phase of that signal and, hence, completely characterize it in the time domain. The phase spectra of the *SV*- and *SH*-components of the Green's function are recovered from the estimates of their respective amplitude spectra, $|G^V(\omega)|$ and $|G^H(\omega)|$, by applying a set of sequential all-pass filters.

The construction of these filters can be accomplished via Kolmogorov spectral factorization (e.g., Claerbout, 1992) of the initial, unprocessed *P*, *SV*, and *SH* seismograms. Defining $\mathcal{K}\{\cdot\}$ as an operator which transforms a time series to minimum phase and exploiting the inherent minimum-phase nature of *P*-component Green's function, $G^P(\omega)$, we write the minimum-phase-transformed *P*-component seismogram as

$$\mathcal{K}\{P_m(\omega)\} = \mathcal{K}\{S_m(\omega)\}G^P(\omega); \tag{5}$$

that is, we generate the seismogram corresponding to a minimum-phase source $\mathcal{K}\{S_m(\omega)\}$ with the same amplitude spectrum as $S_m(\omega)$. Therefore, we define an all-pass filter that rearranges the phase of source *m* to minimum phase as

$$e^{i\phi^S_m(\omega)} = \frac{\mathcal{K}\{P_m(\omega)\}}{P_m(\omega)} = \frac{\mathcal{K}\{S_m(\omega)\}}{S_m(\omega)}. \tag{6}$$

Applying this filter to the *SV* and *SH* seismograms $V(\omega)$ and $H(\omega)$ will likewise transform the source on these components to minimum phase. One subsequent minimum-phase transformation of the resulting time series allows us to define two more all-pass filters, $e^{i\phi^V(\omega)}$ and $e^{i\phi^H(\omega)}$, that transform the nonminimum-phase Green's function components, $G^V(\omega)$ and $G^H(\omega)$, to their minimum-phase counterparts:

$$\begin{aligned} e^{i\phi^V(\omega)} &= \frac{\mathcal{K}\{e^{i\phi^S_m(\omega)}V_m(\omega)\}}{e^{i\phi^S_m(\omega)}V_m(\omega)} \\ &= \frac{\mathcal{K}\{\mathcal{K}\{S_m(\omega)\}G^V(\omega)\}}{\mathcal{K}\{S_m(\omega)\}G^V(\omega)} = \frac{\mathcal{K}\{G^V(\omega)\}}{G^V(\omega)} \end{aligned} \tag{7}$$

and similarly,

$$e^{i\phi^H(\omega)} = \frac{\mathcal{K}\{e^{i\phi^S_m(\omega)}H_m(\omega)\}}{e^{i\phi^S_m(\omega)}H_m(\omega)} = \frac{\mathcal{K}\{G^H(\omega)\}}{G^H(\omega)}. \tag{8}$$

Note that $e^{i\phi^V(\omega)}$ and $e^{i\phi^H(\omega)}$ must be independent of source *m* as they are ultimately defined solely in terms of the Green's function. It is then straightforward to use them to reconstruct the phase of the quantities $|G^V(\omega)|$ and $|G^H(\omega)|$, obtained from solving equation 4 by applying their inverses to the minimum-phase versions of their respective amplitude spectra:

$$G^V(\omega) = e^{-i\phi^V(\omega)}\mathcal{K}\{|G^V(\omega)|\} \tag{9}$$

and

$$G^H(\omega) = e^{-i\phi^H(\omega)}\mathcal{K}\{|G^H(\omega)|\}. \tag{10}$$

In practice, noise will render estimates of $e^{i\phi_V(\omega)}$ and $e^{i\phi_H(\omega)}$, obtained from different seismograms, inconsistent. Therefore, averaging them is likely to improve the accuracy of the filters. Because we are ultimately interested in using the reciprocal quantities to restore the proper phase to the components $G^V(\omega)$ and $G^H(\omega)$ in equations 9 and 10, we construct the averages as

$$A^V(\omega)e^{i\phi^V(\omega)} = \left[\frac{1}{M}\sum_{m=1}^{M} e^{-i\phi^V_m(\omega)}\right]^{-1} \tag{11}$$

and

$$A^H(\omega)e^{i\phi^H(\omega)} = \left[\frac{1}{M}\sum_{m=1}^{M} e^{-i\phi^H_m(\omega)}\right]^{-1}, \tag{12}$$

where $e^{i\phi^V_m(\omega)}$ and $e^{i\phi^H_m(\omega)}$ represent all-pass filters derived from the *m*th seismogram. The all-pass nature of the filters is now lost. However, we can easily show that this choice of average, when applied to equations 9 and 10, leads to a downweighting at frequencies where estimates are least consistent [i.e., $A^V(\omega), A^H(\omega) > 1$], that is, most affected by noise.

## RESULTS

In this section, we demonstrate how the previous deconvolution method can be applied to real three-component teleseismic data successfully to recover three-component Green's functions. We focus on, but do not limit our attention to, the continental crust-mantle boundary, or Moho, and present results from three stations of the CNSN, namely, ULM, WHY, and EDM, which clearly reveal the pure *P* Moho multiple $Pp_Mp$. Before discussing results from real data, we summarize the properties of the principal scattered phases generated by an incident plane *P*-wave within an idealized isotropic layer over a half-space crustal model.

Figure 1a illustrates the raypaths of the first-order scattered phases resulting from interaction between the incident wavefield and the crust-mantle boundary. All these phases are scattered once from the Moho and are recorded on either *P*- or *SV*-components of the teleseismic-*P* Green's function, depending on the nature of their final leg. Figures 1b and c present typical *P*- and *SV*-component Green's function seismograms with the same scattered arrivals identified for the simple crustal model whose physical properties are provided in the caption.

The magnitude and the polarity of the different phases depend both on the reflection and transmission coefficients at the Moho and free surface. The polarities of $P$, $P_Ms$, and $Pp_Ms$ are positive, whereas those of $Pp_Mp$, $Ps_Mp$, and $Ps_Ms$ are negative. The amplitudes of the different first-order scattered phases, excluding $Ps_Mp$, are com-

parable and represent approximately 5% of the incident $P$ amplitude for this value of horizontal slowness or ray parameter. The amplitude of $Ps_Mp$ is somewhat smaller at near-vertical incidence, because this multiple is converted twice en route to the receiver, unlike the other phases that experience, at most, one conversion. We note again that $Pp_Mp$ is the only phase whose amplitude is sensitive to the contrast in compressional modulus (more specifically, the $P$-impedance) at the Moho. All the other phases shown in Figure 1 are sensitive only to combinations of $S$-velocity and density.

Both amplitude and timing of the different phases vary with horizontal slowness (ray parameter). For the narrow range in slownesses represented by teleseismic $=P$ (0.04 – 0.08 s km$^{-1}$), the utility of amplitude versus slowness analysis is limited. It is generally possible, however, to trace the moveout of a given arrival over this slowness band as a useful means of identifying it as either a forward-scattered direct conversion or back-scattered multiple. Figure 4 shows a plot of arrival time, relative to $P$, of the direct $P_Ms$ conversion and the first-order Moho multiples for the simple crustal model described in Figure 1. We note that $P_Ms$ traveltime increases with slowness, while those of the other first-order back-scattered phases decrease. For typical continental crust (as described in Figure 1), $P_Ms$ arrives between 4 and 5 s after direct $P$ followed by $Pp_Mp$ near 10 s on the $P$-component. The kinematic analogues $Ps_Mp$ and $Pp_Ms$ follow near 14 s on separate components with the final first-order scattered phase $Ps_Ms$ coming in close to 19 s.

## Station ULM (Lac du Bonnet, Manitoba)

We now direct attention to the first of CNSN stations. Station ULM is located at Lac du Bonnet, Manitoba, in the western Superior Province of the Canadian Shield. From previous work (Bank and Bostock, 2003), we knew that the site is characterized by a relatively simple, approximately 1D crustal structure. For our analysis, we used seismograms from 344 events representing a wide range of back azimuths. We sorted this data set into 150 equally spaced bins in horizontal slowness between 0.04 to 0.08 s km$^{-1}$ based on the IASPEI reference model (Kennett and Engdahl, 1991). Thus, an average of just more than two seismograms contributed to each bin. All seismograms falling within a given slowness bin then were deconvolved simultaneously to produce Green's function estimates for the corresponding slowness. Each component of the Green's function was filtered between 0.01 and 1.0 Hz and plotted in a 2D image in Figures 5a and 6a where the principal phases were identified according to their timing and moveout. Note that the $P$-component image was muted with a cosine taper between 0 and 1.0 s before filtering to remove the effect of the dominant, incident $P$ arrival.

The $SV$-component Green's function presented in Figure 5a shows coherent signals with timing and moveout corresponding to the three expected, first-order scattered phases from the Moho ($P_Ms$, $Pp_Ms$, $Ps_Ms$). Figure 5b shows the result of stacking these time series along the $P_Ms$, $Pp_Ms$, and $Ps_Ms$ moveout curves defined in Figure 4. These plots further support the interpretation of these scattered

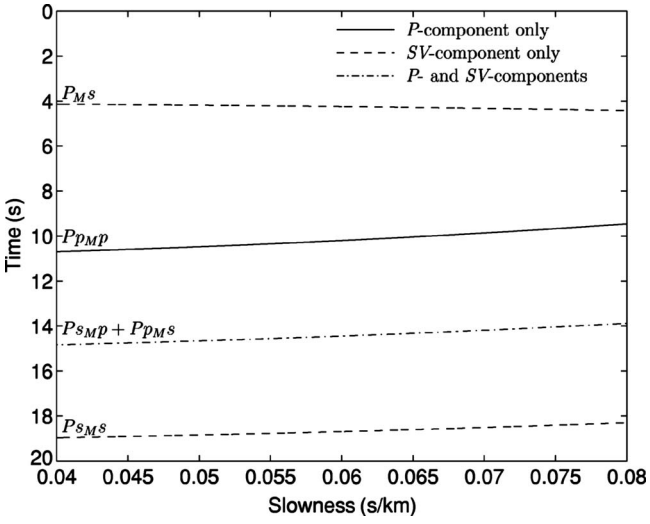


Figure 4. Timing relative to incident $P$ of the first-order crustal scattered phases as a function of slowness for the model described in Figure 1. The curves presented in this diagram are also referred to as moveout curves.

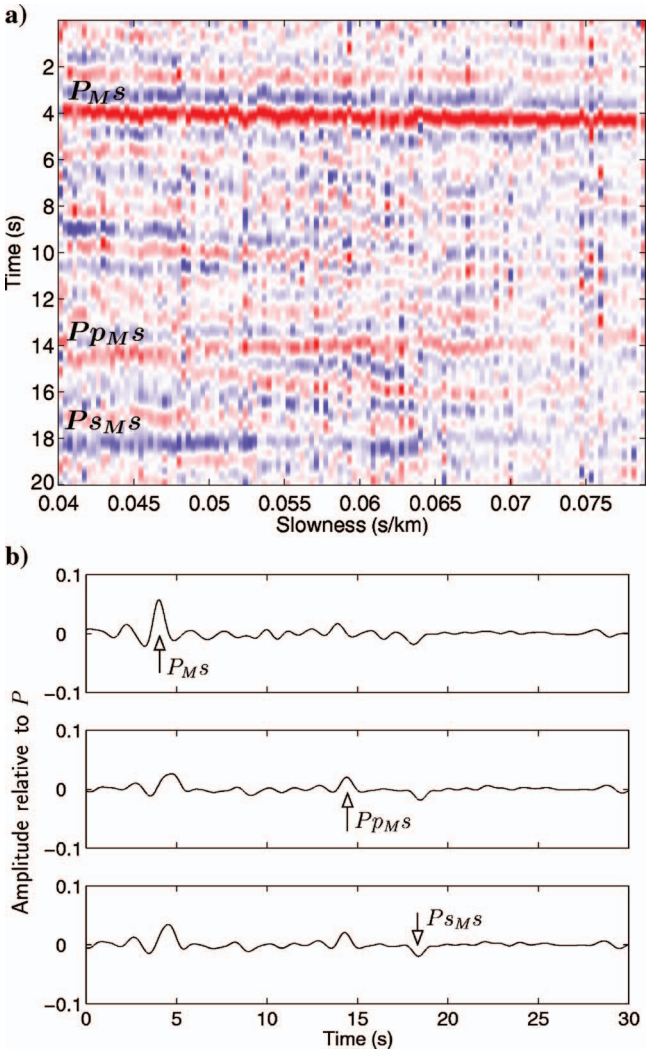


Figure 5. An (a) image of the $SV$-component Green's function as a function of slowness for station ULM and (b) stack along moveout curves of $P_Ms$, $Pp_Ms$, and $Ps_Ms$.

Moho phases with the correct polarization and arrival time, although their relative amplitudes diverged somewhat from expectation. $Pp_Ms$ and $Ps_Ms$ magnitudes are significantly smaller than $P_Ms$ and approximately one-third of those predicted from synthetics obtained using an isotropic, nondissipative model. This discrepancy may be because of energy loss through incoherent scattering and/or intrinsic absorption, or possibly to an extended Moho transition which scatters forward-propagating energy more efficiently than back-scattered energy (Bostock, 1999). We note that a receiver function image would appear very similar to that in Figure 5b because the receiver function is a first-order approximation to the *SV*-component Green's function.

The *P*-component image in Figure 6a also reveals a coherent signal at approximately 10 s following the *P* arrival with negative polarity relative to direct *P*. The signal appears stronger at steep angles of incidence and tends to fade as slowness increases in agreement with theoretical expressions for the reflection coefficient presented by Aki and Richards (1980). The violation of the assumption of 1D structure could contribute also to the diminished signal at larger slowness values. According to its timing and moveout, it can be identified with the receiver-side $Pp_Mp$ multiple. This phase also is evident clearly at the expected arrival time on stacked plots of Figure 6b where a strong negative peak is observed. In contrast, the weaker, reflected-converted $Ps_Mp$ phase is not so clearly defined, either on the 2D image or in Figure 6b. To the best of our knowledge, Figure 6a and b represents the first unambiguous identification of the $Pp_Mp$ phase. We note that other approaches to source estimation and removal from *P*-component seismograms based on stacking of single-event recordings from many stations (Bostock and VanDecar, 1994; Revenaugh, 1995; Li and Nabelek, 1999; Langston and Hammer, 2001) would not have succeeded in isolating the $Pp_Mp$ phase because (1) only data from a single station are available; and (2) signals from near 1D structure, e.g., the Moho, exhibiting little temporal

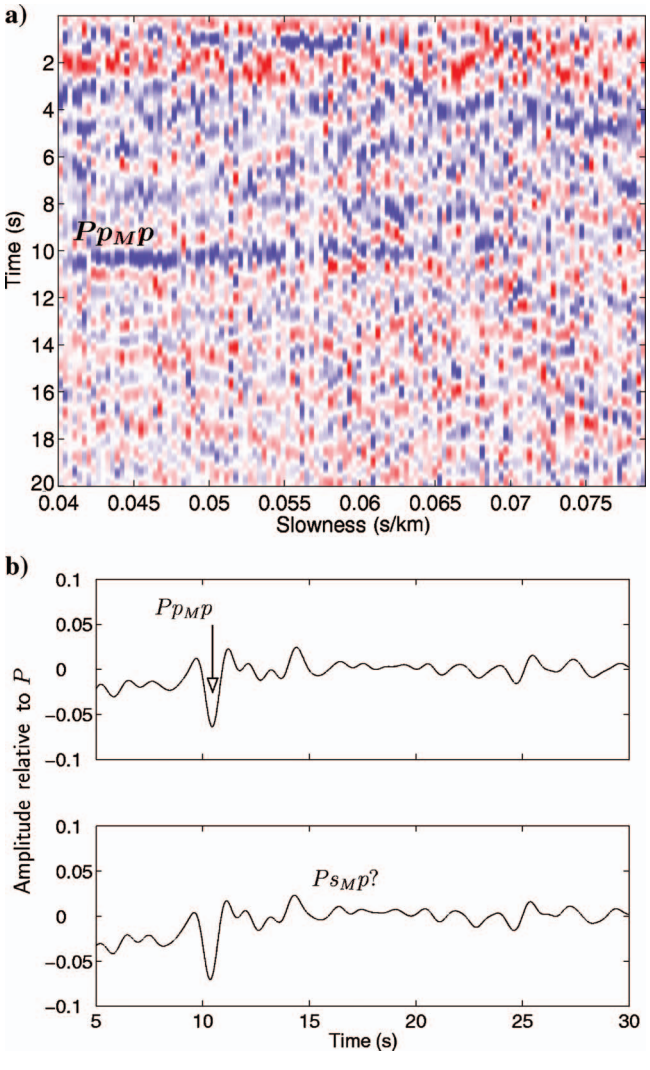


Figure 6. The (a) image of the *P*-component Green's function as a function of slowness for station ULM and (b) stack along moveout curves of $Pp_Mp$ and $Ps_Mp$.

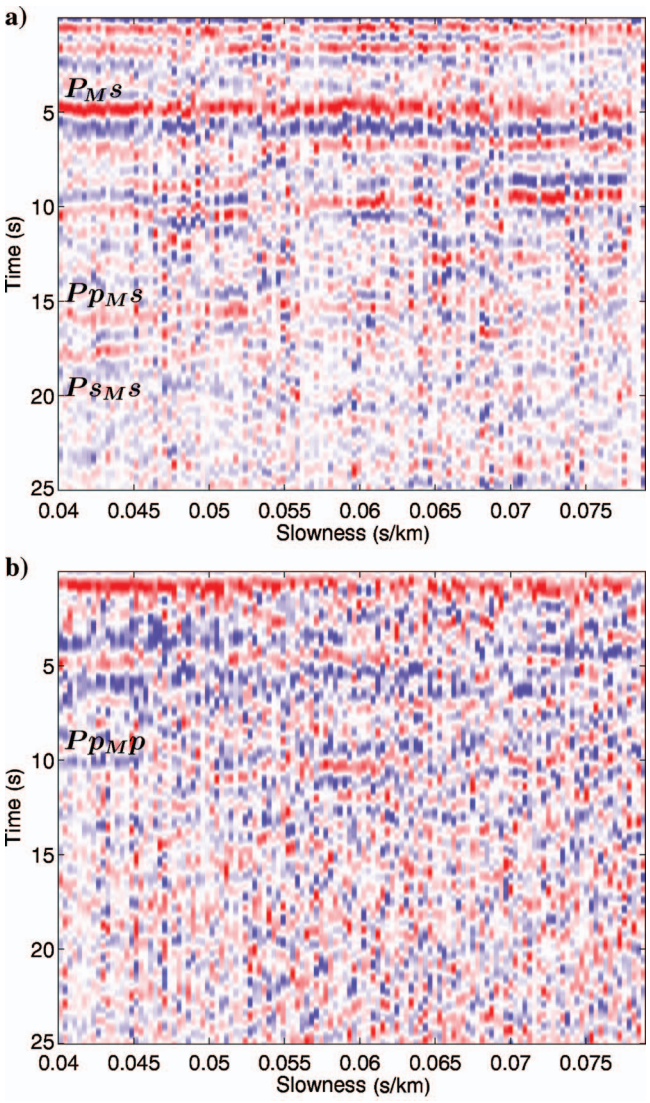


Figure 7. Image of the (a) *SV*-component and (b) *P*-component Green's function as a function of slowness for station WHY.

moveout across stations, will be mapped incorrectly into the source estimate and absent from the recovered Green's functions.

### Station WHY (Whitehorse, Yukon)

Station WHY is situated near Whitehorse, Yukon, within the Cenozoic Canadian Cordilleran orogen (Gabrielse and Yorath, 1992). The images for WHY presented in Figure 7a and b were produced using 415 events, again covering a large range of back azimuths that have been sorted into 150 equally spaced slowness bins and processed similarly to the ULM data set. Unlike ULM, the Moho at this station shows evidence of a more complex crust-mantle boundary.

On the *S*-component image, the $P_Ms$ phase is found between 4 and 5 s with a well-defined moveout and polarization. The main peak is followed immediately by a second negative peak. A comparable signal with opposite moveout and smaller amplitude, interpreted to be the $Pp_Ms$ phase, is observed at 14 s, showing a similar waveform. $Ps_Ms$, which is expected at ~18 s, is not readily apparent on the image. On the *P*-component image, $Pp_Mp$ is clearly defined at 10 s, and like $P_Ms$ and $Pp_Ms$, is composed of two distinct pulses of opposite polarity. This bipolar $P_Ms$ signal was observed previously by Lowe and Cassidy (1995) using a reduced data set. We note that it suggests the presence of a high *P*- and *S*-velocity layer immediately underlying the Moho.

### Station EDM

Station EDM is located near the town of Leduc roughly 25 km to the southwest of Edmonton, Alberta, in the western Canadian Sedimentary Basin. The sedimentary platform in this region is approximately 2.5-km thick (Cassidy, 1995). Our analysis for this station is based on 307 seismograms distributed among 115 equally spaced slowness bins. The data set is processed again using the parameters described for station ULM.

The *P*- and *SV*-component images shown in Figure 8a and b display the usual first-order scattered Moho phases described in preceding sections, albeit the backscattered multiples are rather weak. In addition, there are several signals that clearly originate from shallower crustal levels. As discussed in previous receiver function studies (Cassidy, 1995; Eaton and Cassidy, 1996), these signals result from the basin sediments overlying a crystalline crust that exhibits a pronounced low-velocity zone between 12.5 to 17-km depth.

The sedimentary package (denoted by S) is evident as coherent energy immediately following direct *P* on both components. On the *SV*-component, $P_Ss$ energy associated with the sediments dominates the Green's function for 1.5 s, while its duration on the *P*-component as $Pp_Ss$ extends to 3 s as a result of the longer path length for the multiple. Over this frequency band, it is difficult to discern details of basin structure, but both signals likely are dominated by the scattering from the sediment-basement contact.

The low-velocity zone (denoted by L) appears as the two- or three-lobed signals $Pp_Lp$, $P_Ls$ of opposite polarity on the *P* image near 4 s, and on the *SV* images at approximately 2 s. Eaton and Cassidy (1996) combined receiver function observations with LITHOPROBE crustal-scale reflection data to interpret the layering as serpentinized former oceanic lithosphere thrust up into midcrustal levels during an episode of Proterozoic subduction. Our observation of a coherent $Pp_Lp$ thus bridges a gap in their observations as pure *P* reflections observed at the frequencies of conventional receiver functions.

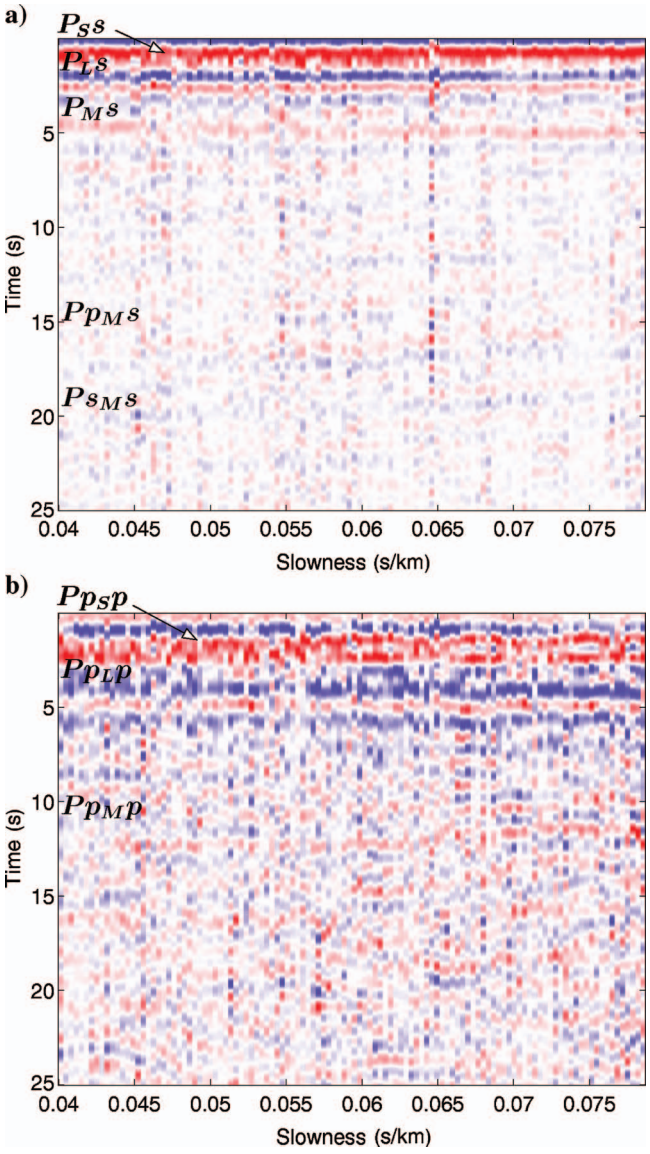


Figure 8. Image of the (a) *SV*-component and (b) *P*-component Green's function as a function of slowness for station EDM. Note the presence of the intracrustal phases (i.e., $P_Ss$, $P_Ls$, $Pp_Sp$, and $Pp_Lp$).

## CONCLUSION

In this paper, we described a new source deconvolution technique that exploits the minimum-phase property of the teleseismic-*P* Green's function to enable recovery, not only of *S*-components, but also the *P*-component of this quantity. We demonstrated that the approach can be applied to real teleseismic data to extract more accurate estimates of the impulse response than those possible using the conventional receiver function approach. In particular, for the first time, we have unambiguously identified and documented the receiver-side $Pp_Mp$ phase from teleseismic observations. The amplitude of this phase provides a measure of the compressional impedance contrast across the crust-mantle boundary, which is not afforded by other signals in the teleseismic $=P$ wavetrain. We note that previous work on extracting *P*-component information from teleseismic *P* generally has involved stacking seismograms recorded at many sta-

tions to produce an approximate source-time function under the assumption that the *P*-coda is incoherent across stations. The main problem with this latter approach is that scattered signals recorded across an array that exhibit little temporal moveout (e.g., the $Pp_MP$ phase in many instances) are mapped incorrectly to the source and are thus absent from the resulting Green's function. As we have demonstrated, our approach does not suffer from this shortcoming.

We present results for three stations of the CNSN, each representing a different geologic environment. Each station, namely ULM (Lac du Bonnet, Manitoba), WHY (Whitehorse, Yukon), and EDM (Edmonton, Alberta), shows evidence of the principal, first-order scattered Moho phases and, in particular, the $Pp_MP$ multiple. Station ULM exhibits a very simple crustal structure that is reasonably well modeled as a layer over a half-space. The crust-mantle boundary at station WHY, as portrayed through $P_MS$ and $Pp_MP$, is revealed to be more complex, representing a thin, high-velocity lid. Intra-crustal scattering dominates the Green's functions recovered at station EDM. The sedimentary-basement contact produces prominent arrivals at early times followed by signals from a pronounced low-velocity layer that has been previously interpreted from seismic reflection and receiver functions to represent a serpentinized sliver upthrust during Proterozoic subduction.

## ACKNOWLEDGMENTS

We are grateful to referees Charles Langston and Gary Pavlis for their constructive reviews and to guest editors Kees Wapenaar and Deyan Draganov for the invitation to contribute to this volume. This research was supported by Natural Sciences and Engineering Research Council of Canada grant RGPIN 138004-2000.

## REFERENCES

Aki, K., and P. G. Richards, 1980, Quantitative seismology, theory and methods: vol. 1: W. H. Freeman and Company.

Andrews, D. J., 1986, Objective determination of source parameters and similarity of earthquakes of different sizes, 37th ed.: American Geophysical Union.

Baig, A. M., M. G. Bostock, and J.-P. Mercier, 2005, Spectral reconstruction of teleseismic-P Green's functions: Journal of Geophysical Research, **110**, B08306,

Bank, C.-G., and M. G. Bostock, 2003, Linearized inverse scattering of teleseismic waves for anisotropic crust and mantle structure: 2. Numerical examples and application to data from Canadian stations: Journal of Geophysical Research, **108**, 2259,

Bostock, M. G., 1999, Seismic waves converted from velocity gradient anomalies in the Earth's upper mantle: Geophysical Journal International, **138**, 747–756.

——, 2004, Green's functions, source signatures, and the normalization of teleseismic wave fields: Journal of Geophysical Research, **109**, B03303,

Bostock, M. G., S. Rondenay, and J. Shragge, 2001, Multiparameter two-dimensional inversion of scattered teleseismic body waves: 1. Theory for oblique incidence: Journal of Geophysical Research, **106**, 30771–30782.

Bostock, M. G., and J. C. VanDecar, 1994, The influence of crust and upper mantle heterogeneity on short period waveform distortion: Physics of the Earth and Planetary Interiors, **83**, 225–247.

Burdick, L. J., and C. A. Langston, 1977, Modeling crustal structure through the use of converted phases in teleseismic body-wave forms: Bulletin of the Seismological Society of America, **67**, 677–691.

Cassidy, J. F., 1995, A comparison of the receiver structure beneath stations of the Canadian National Seismograph Network: Canadian Journal of Earth Sciences, **32**, 938–951.

Claerbout, J., 1992, Earth sounding analysis: Processing versus inversion: Blackwell Scientific Publications Inc.

Dueker, K. G., and A. F. Sheehan, 1997, Mantle discontinuity structure from midpoint stacks of converted P and S waves across the Yellowstone hotspot track: Journal of Geophysical Research, **102**, 8313–8326.

Eaton, W. E., and J. F. Cassidy, 1996, A relic Proterozoic subduction zone in western Canada: New evidence from seismic reflection and receiver function data: Geophysical Research Letters, **23**, 3791–3794.

Gabrielse, H., and C. Yorath, eds., 1992, Geology of the cordilleran orogen in Canada, vol. 4: Geological Survey of Canada.

Kennett, B. L. N., 1991, The removal of free surface interactions from three-component seismograms: Geophysical Journal International, **104**, 153–163.

Kennett, B. L. N., and E. R. Engdahl, 1991, Traveltimes for global earthquake location and phase identification: Geophysical Journal International, **105**, 429–465.

Langston, C. A., 1979, Structure under Mount Rainier, Washington, inferred from teleseismic body waves: Journal of Geophysical Research, **84**, 4749–4762.

Langston, C. A., and J. K. Hammer, 2001, The vertical component P-wave receiver function: Bulletin of the Seismological Society of America, **91**, 1805–1819.

Li, X.-Q., and J. L. Nabelek, 1999, Deconvolution of teleseismic body waves for enhancing structure beneath a seismometer array: Bulletin of the Seismological Society of America, **89**, 190–201.

Lowe, C., and J. F. Cassidy, 1995, Geophysical evidence for crustal thickness variations between the Denali and Tintina fault systems in west-central Yukon: Tectonics, **14**, 909–917.

Owens, T. J., and G. Zandt, 1985, The response of the continental crust-mantle boundary observed on broadband teleseismic receiver functions: Geophysical Research Letters, **12**, 705–708.

Phinney, R. A., 1964, Structure of the Earth's crust from spectral behavior of long-period body waves: Journal of Geophysical Research, **69**, 2997–3017.

Poppeliers, C., and G. L. Pavlis, 2003, Three-dimensional, prestack, plane wave migration of teleseismic P-to-S converted phases: Journal of Geophysical Research, **108**, 2112,

Revenaugh, J. A., 1995, Scattered-wave image of subduction beneath the Transverse Ranges, California: Science, **268**, 1888–1892.

Sherwood, J. W. C., and A. W. Trorey, 1965, Minimum-phase and related properties of a horizontally stratified absorptive Earth to plane acoustic waves: Geophysics, **30**, 191–197.

Vinnik, L. P., 1977, Detection of waves converted from P to SV in the mantle: Physics of the Earth and Planetary Interiors, **67**, 39–45.

Zandt, G., and J. A. Ammon, 1995, Continental crust composition constrained by measurements of crustal Poisson's ratio: Nature, **374**, 152–154.

Zhu, L., and H. Kanamori, 2000, Moho depth variation in southern California from teleseismic receiver functions: Journal of Geophysical Research, **105**, 2969–2980.